Check for updates

Morphology does not matter: WSe$_2$ luminescence nanothermometry unravelled†

Paloma Martínez-Merino,*[a] Miguel A. Hernández-Rodríguez, [ID] [b,c]
José C. Piñero, [ID] [d] Carlos D. S. Brites, [ID] *[c] Rodrigo Alcántara [ID] *[a] and
Javier Navas [ID] *[a]

Transition metal dichalcogenides, including WSe$_2$, have gained significant attention as promising nano-materials for various applications due to their unique properties. In this study, we explore the temperature-dependent photoluminescent properties of WSe$_2$ nanomaterials to investigate their potential as luminescent nanothermometers. We compare the performance of WSe$_2$ quantum dots and nanorods synthesized using sonication synthesis and hot injection methods. Our results show a distinct temperature dependence of the photoluminescence, and conventional ratiometric luminescence thermometry demonstrates comparable relative thermal sensitivity (0.68–0.80% K^{-1}) and temperature uncertainty (1.3–1.5 K), irrespective of the morphology of the nanomaterials. By applying multiple linear regression to WSe$_2$ quantum dots, we achieve enhanced thermal sensitivity (30% K^{-1}) and reduced temperature uncertainty (0.1 K), highlighting the potential of WSe$_2$ as a versatile nanothermometer for microfluidics, nanofluidics, and biomedical assays.

Introduction

Transition metal dichalcogenides (TMDCs) are a family of inorganic compounds of formula MX$_2$ in which M refers to a transition metal (groups from 4 to 10) and X to a chalcogenide.[1–4] Most of these compounds crystallize in a graphite-like layered structure, with each monolayer consisting of a hexagonal layer of metal atoms sandwiched between two layers of chalcogenide atoms. The intralayer M–X bonds are covalent but the neighbouring atomic layers are held together by weak van der Waals forces.[5,6] These weak interlayer interactions allow the bulk material to be exfoliated into two-dimensional layers of single-unit cell thickness.[3,7] 2D layered TMDCs materials have attracted considerable interest because, in their monolayer form, they exhibit interesting and unique properties compared to bulk material due to confinement effects.[8] For example, as the thickness of the TMDCs is reduced from bulk to single layer, there is a transition from indirect bandgap to direct bandgap, resulting in significant increases in photoluminescence.[9–11] This characteristic makes these compounds interesting for many optoelectronic applications such as phototransistors, LEDs, photodetectors, and solar cells.[12–14] To date, the photoluminescence properties of these materials have not been investigated for luminescence (nano)thermometry.[15]

Nanothermometry is a technique aiming at determining the temperature of a sample with a sub-micrometer spatial resolution.[15–17] This is of great interest in diverse fields of nanotechnology and biomedicine since temperature is a critical parameter affecting the performance of any device and plays a pivotal role in many cellular processes.[18] For example, cancer cells, because of their faster metabolism, tend to have higher intracellular temperatures than healthy ones.[19,20] In addition, temperature provides information on cell division rates and the response of tissues to external interactions.[21] Accurate control of cell and tissue temperatures is also essential during hyperthermia therapy, in which cancer cells are destroyed by heating.[22] Therefore, precise temperature monitoring becomes crucial for gaining insights into biological systems and for the development of biomedical therapies.

One of the most relevant approaches to nanothermometry is *via* luminescent nanoprobes.[15,16] This technique uses the temperature-dependent photophysical properties of a luminescent material to determine the temperature in a remote detection scheme. Luminescence nanothermometry probes consti-

*[a]Departamento de Química Física, Facultad de Ciencias, Universidad de Cádiz, E-11510 Puerto Real, Cádiz, Spain.
E-mail: paloma.martinez@uca.es, rodrigo.alcantara@uca.es, javier.navas@uca.es*
[b]Departamento de Física, Universidad de La Laguna, Apdo. Correos 456, E-38200 San Cristóbal de La Laguna, Santa Cruz de Tenerife, Spain
[c]Phantom-g, CICECO – Aveiro Institute of Materials, Department of Physics, University of Aveiro, 3810-193 Aveiro, Portugal. E-mail: carlos.brites@ua.pt
[d]Departamento de Didáctica (Área de Matemáticas), Universidad de Cádiz, E-11510 Puerto Real, Spain
†Electronic supplementary information (ESI) available. See DOI: https://doi.org/10.1039/d4nr00014e

tuted of organic dyes,[23,24] quantum dots (QDs),[25,26] metal nanoparticles,[27,28] rare-earth-doped nanoparticles,[29,30] and polymers[31,32] have been reported. However, it is a challenge to develop materials that link diverse requirements such as high photostability, thermal and chemical stability, and sometimes low cytotoxicity (*e.g.*, for biomedical applications), with high thermometric performance, quantified by the relative thermal sensitivity and temperature uncertainty.[33] For example, the first application of luminescent probes to access the temperature was applied to $Zn_{1-x}Cd_xS$ by Urbach *et al.* in 1949,[34] reporting applications in aeronautics[35] and medicine[36] in the 1950s and the 1960s. Later, in 2009 Han *et al.*[37] first reported the use of CdSe QDs to monitor the temperature of cancer cells, achieving sub-degree thermal resolution from the measurement of fluorescence intensity. The physical principle of operation in these examples was the thermal quenching of the luminescence. However, Maestro *et al.*[38] succeeded in measuring intracellular temperature using a shifting of position of the emission band of CdSe QDs. Nonetheless, the toxicity of Cd-based QDs remains a major concern for their use in biological systems.[39,40] Recently Ag_2S nanocrystals emerged in the community showing great potential as luminescent nanothermometers.[41] However, their relative thermal sensitivity is highly dependent on the surrounding environment.[42] Additionally, QD-polymer composite films have been found to suffer from poor thermal stability due to changes in polymer morphology with thermal aging.[43] As a result, there is still an increasing need to explore and develop alternative compounds that can serve as safe and effective nanothermometers for biomedical applications.

Multiple linear regression (MLR) is a powerful numerical technique that finds extensive applications in sensing, particularly in the field of luminescence sensing.[44,45] MLR enables to explore intricate relationships between multiple predictor variables and a response variable, providing valuable insights into the sensing process. In the context of luminescence thermal sensing, MLR allows to incorporate various parameters affecting the response of the luminescent materials to changes in the sensing environmental temperature yielding better performance parameters, typically one order of magnitude higher than the analysis of a single thermometric parameter alone.[44,46]

Here we investigate the use of WSe_2 nanomaterials as luminescent nanothermometers exploring their temperature-dependent photoluminescent properties. We use these nanomaterials to investigate the influence of their morphology on the corresponding thermometric performance. As WSe_2 belongs to the family of transition metal dichalcogenides, strong luminescence at the nanoscale is expected. Furthermore, previous studies have reported low cytotoxicity of WSe_2 compared to other nanomaterials like graphene oxide.[47] In this work, we compare the temperature-dependent photoluminescent properties of QDs and nanorods (NRs) of WSe_2. Both samples were prepared using fast and simple synthetic procedures, with the QDs synthesized by sonication and the NRs prepared using the hot injection method. We compare the

performance of the luminescent materials as remote thermometers using the conventional single thermometric parameter and multiple parametric approaches, yielding an improvement in the relative thermal sensitivity and temperature resolution by one order of magnitude. We conclude that no significative changes were observed in the thermometric performance of the material when the morphology and size of the luminescent nanothermometers are modified, for WSe_2 nanomaterials. Our findings could pave the way for a new class of nanothermometers based on Pb-free WSe_2 materials that may find application in micro and nanofluidic and also for biomedical assays, irrespective of theira morphology.

Results and discussion

Structural characterization

The synthesis of WSe_2 QDs (**1**) and WSe_2 NRs, (**2**) is described in detail in the Experimental section. The samples were observed in a transmission electronic microscope (TEM). Fig. 1a shows the TEM image of **1**. There are WSe_2 QDs of sizes between 3–11 nm, with an average size of 4 ± 1 nm. The same analysis for **2** permits to observe WSe_2 NRs.

Fig. 1b shows the TEM image of **2**. Nanorods with length of 18 ± 5 nm and diameter of 4 ± 1 nm are observed. The size distributions were accessed by a statistical analysis performed on the TEM images. The resulting histogram of diameter (for **1**) and length and diameter (for **2**) were find by fitting to log–normal distributions using OriginLab® software (Fig. 1c and
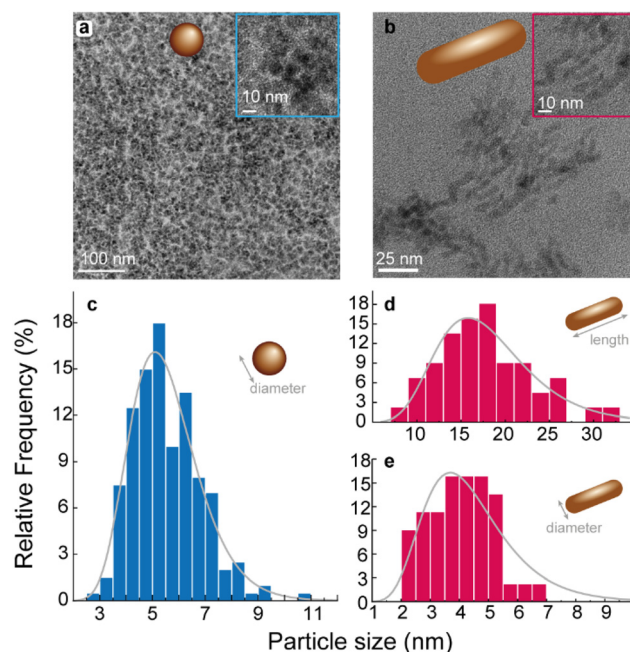

Fig. 1 TEM images and size distribution of (a) **1** and (b) **2**. The corresponding size distributions are presented in (c) and (d). The lines are the best fit to the histogram of sizes using a log−normal curve ($r^2 > 0.994$). The fitting results are presented in Table S1 in ESI.†

d). The values of the parameters of these distributions are presented in Table S1 in ESI.†

In addition, TEM analysis was used to explore the crystalline configuration of the different samples. High-resolution Bright Field images were acquired for both samples, showing in Fig. 2a TEM image representative. QDs and NRs were randomly oriented, and a search for well-aligned nanoparticles (with respect to the incident beam) was carried out. Some of the randomly oriented nanoparticles showed an orientation that allows for a High-Resolution Electron Microscopy (HREM) analysis, as highlighted by the blue-dashed square in Fig. 2a. Thus, HREM micrography was obtained and is shown in Fig. 2b, inset shows a detail of the blue-dashed area where atomic columns are evidenced.

Fourier Transform of Fig. 2b provides a selected area diffraction pattern (SAED), as presented in Fig. 2c. Once the diffraction pattern is indexed, zone axis (ZA) 100 of a hexagonal $P6_3/mmc$ lattice is identified, which confirms the preparation of crystalline 2H phase of WSe_2.[48] The corresponding diffraction spots were indexed and its corresponding Miller indexes are indicated in Fig. 2c. Moreover, theoretical interplanar distance on the 010 direction (d_{010}) was calculated by using eqn (S1) in ESI,† obtaining d_{010} = 3.8 Å, assuming that the hexagonal lattice parameters of a WSe_2 NP are $a = b$ = 3.32 Å and c = 13.74 Å.[49] The interplanar distance measured in Fig. 2b (orange arrows), d_{010} = 3.73 Å, is indeed in close agreement with the calculated value. The data yielded by this analysis provides convincing evidence that the samples well fit WSe_2 with a lattice corresponding to the $P6_3/mmc$ space group.

In addition, the size of the nanomaterials was analyzed by dynamic light scattering obtaining a hydrodynamic diameter
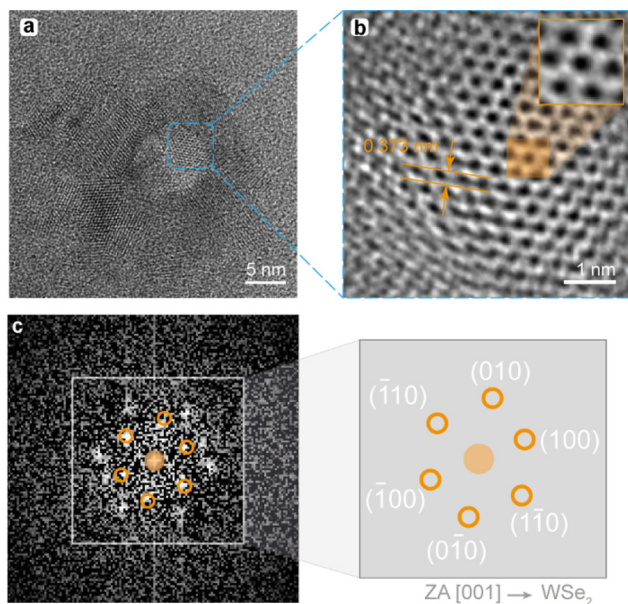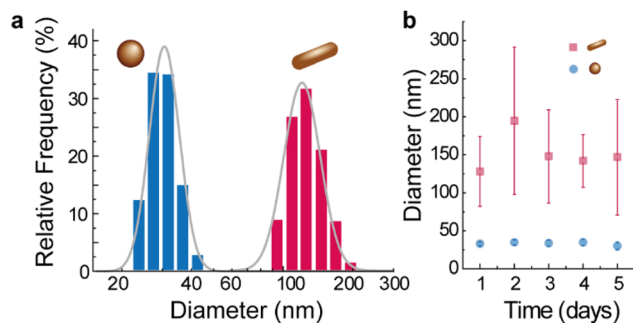

Fig. 3 (a) Hydrodynamic diameter of **1** and **2**. The solid lines are the best fits to log–normal curves (r^2 > 0.991, see Table S2 in ESI†). (b) Time evolution of the hydrodynamic diameter of the nanomaterials.

of 32.9 ± 2.4 nm for **1** and 128 ± 45.8 nm for **2** as shown in Fig. 3a. The hydrodynamic diameter distributions are well described by log–normal functions for both materials (Table S2 in ESI†), which remain constant over time within the uncertainties (Fig. 3b), attesting their colloidal stability.

Photoluminescence

The absorption spectra of **1** and **2** (Fig. S1 in ESI†) show absorption at 300 and 400 nm in the NRs sample, while the absorption of the QDs extends up to 500 nm. WSe_2 has been studied for its absorption properties in the visible (VIS) range. In the literature it is shown that these observations are related to the electronic structure of WSe_2, probed using high-resolution angle-resolved photoelectron spectroscopy.[50] Ding *et al.* show a dominantly electron-like Fermi surface and a shift in the low-energy band structures at room temperature.[50] Additionally, the interlayer charge transfer in WSe_2 heterostructures has been studied, revealing efficient charge transfer between WSe_2 and MoS_2.[50,51] The excitation spectra of the samples, presented in Fig. S2 in ESI,† show that the samples are excitable in the UV-VIS spectral range. The emission spectra of samples **1** and **2** are shown in Fig. S3 and S4 in ESI.† There is a redshift from about 360 to 460 nm for **1** and from 350 to 450 nm for **2**. This shift is typical from TMDCs and was reported previously in carbon dots,[52] MoS_2 QDs[53,54] or graphene QDs[55,56] samples, being attributed in some cases also to the wide size distribution and to surface trap states in QDs.[57,58] The origin of these observations is still not fully understood, despite recent characterization efforts by Bora *et al.* suggesting the key role of direct gap transitions and defect-bound excitons.[59] It was reported that the excitation wavelength influences spectral properties, indicating selective excitation-recombination at specific energy levels plays an important role.[59] This discussion lies, however, outside the scope of the present work, and will be investigated in detail in future publications.

Looking forward to the application of these materials to luminescence thermometry, we record the emission spectra at different temperatures of a dispersion of **1** in polyethylene glycol 400 (Fig. 4a) and of **2** in oleylamine and ethanol (Fig. S4

Fig. 2 (a) Bright field micrography of a representative WSe_2 particle. (b) HREM imaging of a section, inset shows a detail where atomic columns can be evidenced. (c) Indexed diffraction pattern of the (b) region.
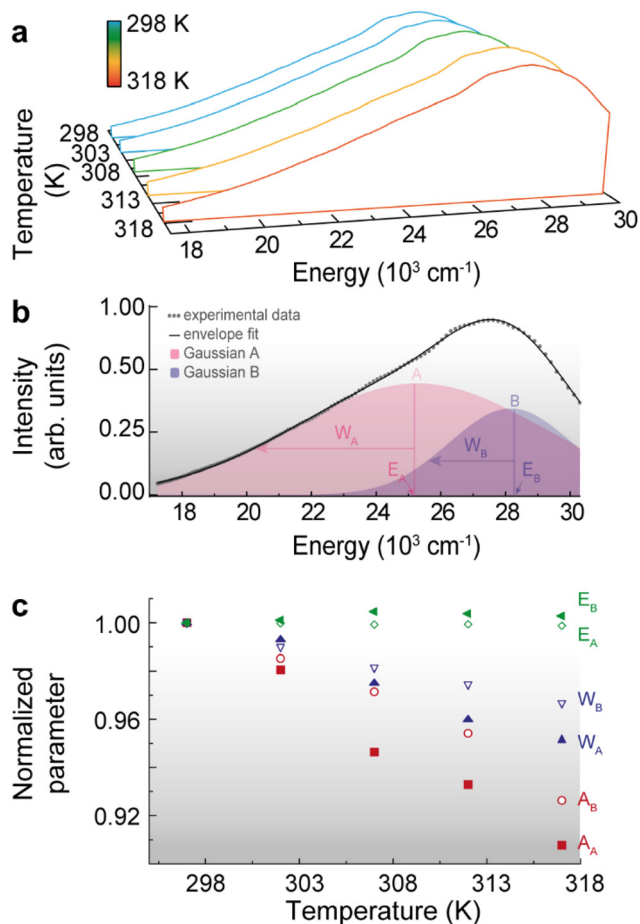
Fig. 4 (a) Emission spectra of **1** upon 310 nm excitation in the 298–318 K range. (b) Illustration of the deconvolution procedure for **1** at 298 K, implemented in MatLab®. The Gaussian components of higher and lower energy are identified by A and B, respectively. The parameters of the deconvolution are given in Table S4 in ESI.† (c) Temperature dependence of the normalized integrated area (A_i), width (W_i) and peak energy (E_i) for the i = A, B Gaussian components.

in ESI†). The emission spectra present a distinct temperature dependence that can be rationalized as the contribution of two distinct components. Experimental results on the origin of the temperature dependence of the photoluminescence properties lies out of the scope of the present paper, however, Oreszczuk et al.[60] reported a non-instantaneous rise in the emission intensity after an excitation laser pulse in few-layer WSe₂ materials. The authors concluded that the simple excitation model of direct population of localized states by free excitons is not sufficient and that their lifetimes are strongly suppressed by temperature increase, and, thus a more complex model involving long-lived intermediate states may be aplicable.[60]

For the emission spectra analysis, we employ a deconvolution technique using two Gaussian components (A and B), each representing a distinct contribution to the overall signal (Fig. 4b). By fitting the experimental data to this deconvolution model, we estimate the parameters of each Gaussian component i = A, B, namely the peak energy (E_i), width (W_i), and

integrated area (A_i), as is shown in Table S3 in ESI.† This approach enables us to disentangle the overlapping contributions, providing valuable insights into the underlying processes or components responsible for the observed emission spectrum, constituting a valuable tool for characterizing and understanding complex emission spectra in our study. The deconvolution parameters were normalized to their values at the lowest temperature to evaluate the relative change of each parameter with the temperature (Fig. 4c). Whereas the peak energy E_i values remain essentially constant with the temperature increase, both the integrated area and peak width decrease with the temperature increase. The thermal quenching phenomenon is here evident and involves a decrease in the areas (A_i) associated with a specific component in the emission spectra as the temperature increases. This reduction in the area indicates a decrease in the emission intensity or efficiency of the corresponding component, likely due to enhanced nonradiative processes, such as phonon-assisted energy dissipation or defect-mediated mechanisms.[61]

The decrease of transition widths (W_i) in WSe₂ nanomaterials with increasing temperature can be attributed to a complex interplay of factors,[62–64] however, we attribute the observed reduction of bandwidth to the reduction of inhomogeneous broadening, as discussed before for nanocrystalline ZnS:Mn²⁺ materials.[65]

Conventional ratiometric luminescence thermometry

Looking forward to the implementation of a conventional luminescent thermometer we analyse the ratio of the areas of the transitions $\Delta = A_A/A_B$ as the thermometric parameter for both **1** and **2** samples. The ratiometric definition allow us to follow the temperature irrespectively of eventual optoelectronic or detection fluctuations. (Fig. 5) presents the calibration curves and performance parameters for **1** and **2**. In the absence of a theoretical background for Δ, we adopt a phenomenological straight line calibration curve, whose parameters are shown in Table S4 in ESI.† The corresponding relative thermal sensitivity (S_r) ranges between 0.68 and 0.80% K⁻¹ for **1** and 0.58 and 0.66% K⁻¹ for **2**. The corresponding temperature uncertainties are of 1.3 to 1.5 for **1** and 1.5 and 1.7% K⁻¹ for **2**. These values are comparable with those found in the literature on transition metal dichalcogenides,[60] QDs,[61] and nanowires[33] (Table S5 in ESI†).

Improved performance using multiple linear regression

A recent study presented a comprehensive application of MLR to the field of luminescent nanothermometry. This numerical technique significantly enhances the sensitivity and decrease the temperature uncertainty by combining several temperature-dependent features of EGFP. This approach leads to an impressive 10-fold increase in thermal sensitivity, surpassing the limitations of single-parameter sensing. Additionally, the study demonstrates the remarkable potential of MLR in the analysis of Ag₂S nanoparticles, as it enables a record-breaking relative thermal sensitivity of 50% K⁻¹ during in vivo measurements. Importantly, MLR achieves these advancements
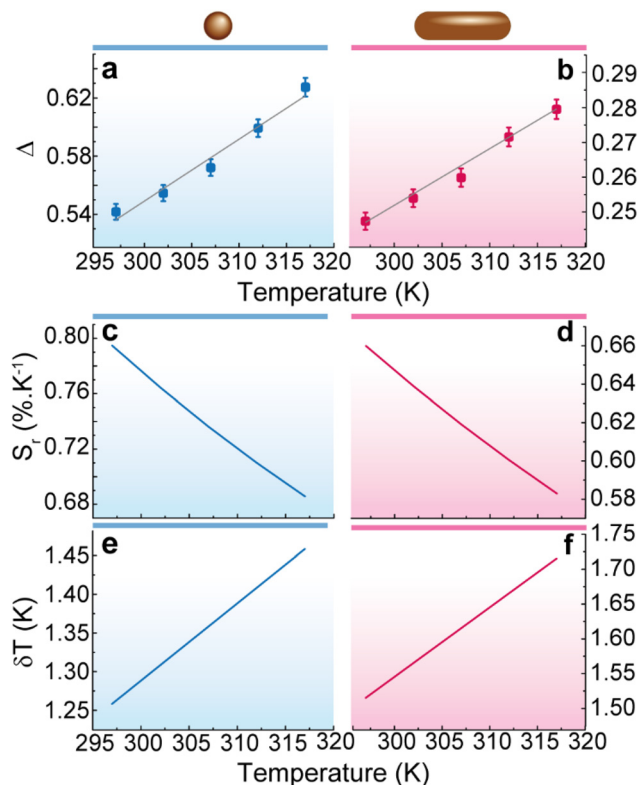
Fig. 5 Thermal calibration curve for (a) **1** and (b) **2**. The lines are the best fits to straight lines (fitting parameters in Table S3 in ESI†). Relative thermal sensitivity for (c) **1** and (d) **2**. Temperature uncertainty for (e) **1** and (f) **2**.

without necessitating complex system upgrades or material design modifications. These findings highlight the effectiveness of MLR as a valuable strategy for advancing luminescent nanothermometry and its broader scientific applications. Inspired by these results here we apply MLR analysis to the emission features of QDs and NRs. As an illustrative example, we exploit **1** as it presents the better performance parameters for a single-variable analysis, as described in the previous section.

(Fig. 6) presents the MLR analysis for **1**. The details of the MLR analysis are presented in Experimental section. The four selected thermometric parameters, W_A, W_B, A_A and A_B present a linear dependence in the studied temperature range (Fig. 4c). Notice that the peak energy (E_i) values were not considered as they faintly depend on the temperature. The combination of these parameters was performed as detailed in the literature and the β-weighting were calculated (Fig. 6a).

It is interesting to notice that the lowest temperature dependence for the parameters W_A and W_B is compensated by the algorithm with higher β-weights, balancing the contributions of all the parameters for the estimation of the temperature. As reported before, this numerical strategy improves the thermal performance of the material by one order of magnitude, yielding a maximum relative thermal sensitivity of 10% K^{-1} and a minimum temperature uncertainty of about 0.1 K (Fig. 6).
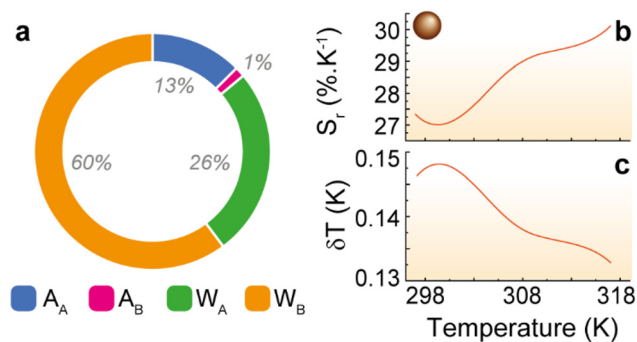

Fig. 6 Multiple linear regression analysis for **1**. (a) Doughnut plot of the β-weights for the distinct parameters used in the MLR. (b) Relative thermal sensitivity and (c) temperature uncertainty of **1** in the 298–318 K range.

Reproducibility assessment

To test the temperature stability of these samples, temperature cycling was performed by measuring the photoluminescence of the samples at 32 °C and 45 °C five times. Fig. S6† shows that the variation of the photoluminescent signal of both WSe_2 QDs and WSe_2 NRs samples is negligible after each cycle. The peak of the photoluminescent emission in each cycle has been plotted in Fig. S7 in ESI.† The results revealed that the peak intensity only varies by 1.7% in the case of WSe_2 QDs (Fig. S7a†) and 3.3% in the case of WSe_2 NRs (Fig. S7b†). The Δ parameter (Fig. S7c and S7d†), understood as the difference in intensities at low and high temperatures changes most between the first two cycles (7.7% in QDs and 2.8 in NRs between cycles 1 and 2) and then the difference is smaller (4.2% in QDs) or non-existent (NRs) between cycles 2 and 3. These results indicate the possibility of using these samples for several times as nanothermometers due to their high thermal stability.

Experimental

Materials

For the synthesis of WSe_2 QDs, the reagents used were WSe_2 (powder 10–20 μm, purity ~99.8%, Alfa Aesar) and polyethylene glycol 400 (PEG, MW 380–420, Panreac). In the case of WSe_2 NRs, tungsten hexcarbonyl $W(CO)_6$ (97.0%), oleylamine (70.0%), Se (powder, −100 mesh, ≥99.5% trace metals) and toluene (99.8%) were provided by Sigma Aldrich. Absolute ethanol (99.8%) was supplied by Honeywell.

Synthesis of WSe_2 quantum dots, sample 1

In the sonication synthesis method of WSe_2 QDs, 0.05 g of bulk WSe_2 was dispersed in 50 ml of PEG-400. The dispersion was sonicated in a Bandelin Sonopuls HD 4200 sonicator for an effective time of 12 h at a frequency of 40% and using a sonication pulse of 1 s *on* and 2 s *off*. Subsequently, the suspension was centrifuged at 10 000 rpm for 10 min. Finally, the

supernatant liquid obtained constitutes the colloidal dispersion of WSe_2 QDs in PEG-400.

Synthesis of WSe_2 nanorods, sample 2

In a typical hot injection process,[66] 0.070 g $W(CO)_6$ and 8 mL oleic acid were added to a three-necked flask. The mixture was kept under vacuum for 1 h at room temperature and then at 80 °C for 20 minutes. In the meantime, 0.063 g of Se was dispersed in 2 mL of oleic acid in a vial. After the degassing process of the tungsten precursor, the mixture was heated to 300 °C under a nitrogen flow. When this temperature was reached, the mixture of Se and oleic acid was rapidly injected into the flask and the reaction was maintained for 2 minutes. Then, the solution was cooled to room temperature. 5 mL of ethanol was added to the flask and the suspension was centrifuged for 10 min at 10 000 rpm. The precipitate was washed several times with toluene and ethanol.

Characterization

The morphology and crystalline configuration of the samples was characterized by Transmission Electron Microscopy using a FEI Talos™ F200S microscope. Hydrodynamic particle size measurements were also performed using the dynamic light scattering (DLS) technique by means of a Zetasizer Nano ZS system supplied by Malvern Instruments Ltd. UV-VIS absorption spectra were recorded on a PerkinElmer Lambda 950 UV-VIS/NIR spectrometer. Photoluminescence (PL) spectra were obtained at room temperature using a Fluorolog3® Horiba Scientific (Model FL3-22) spectroscope, with a modular double grating excitation spectrometer (fitted with a 1200 grooves per mm grating blazed at 330 nm) and a TRIAX 320 single emission monochromator (fitted with a 1200 grooves per mm grating blazed at 500 nm, reciprocal linear density of 2.6 nm mm^{-1}) in the front face mode. The excitation source was a 450 W Xe arc lamp. The temperature-dependent measurements were performed attaching a home-made Peltier temperature controller (0.1 K resolution) to the abovementioned setup. The emission spectra were corrected with the spectrofluorimeter optical spectral response and the spectral distribution of the lamp intensity using a photodiode reference detector, respectively. The calibration of temperature was performed by using a K-type thermocouple with a temperature uncertainty of 0.1 K (KA01-3, TME Thermometers) coupled to a thermocouple data logger (TC-08, Pico Technology).

Deconvolution procedure

The Gaussian deconvolution procedure was implemented in MatLab®. Each spectrum is fitted using a two-component Gaussian model. To prepare the data, a Jacobian transformation is applied to convert the wavelength to energy. The deconvolution is performed iteratively for each temperature, extracting the integrated area (A_i), peak energy (E_i), and width (W_i) of the two Gaussian components (i = A, B).

Multiple linear regression

The multiple linear regression procedure was implemented in Excel using the datapoints of integrated area (A_i) and width (W_i) of the two Gaussian components (i = A, B) obtained from the deconvolution procedure.

Thermometric performance

The relative thermal sensitivity (S_r) and the temperature uncertainty (δT) were calculated using the definitions presented in ref. 44.

Conclusions

Here we present a comprehensive study on the luminescent properties of WeS_2 QDs and NRs for applications in luminescence thermometry. Through detailed analysis of their emission spectra, we have observed distinct temperature-dependent photoluminescent properties, that can be attributed to various factors, including the size distribution and surface trap states in the QDs. Our investigation revealed that the emission spectra of both WeS_2 QDs and NRs exhibited a temperature-dependent photoluminescent properties that were analyzed by a deconvolution technique utilizing two Gaussian components to disentangle the overlapping contributions in the emission spectra. This approach allowed us to estimate parameters such as peak energy, width, and integrated area, providing valuable insights into the underlying processes responsible for the observed emission spectra. Furthermore, we explored conventional ratiometric luminescence thermometry as a potential method for temperature sensing, which involves analysing the ratio of the areas of distinct transitions in the emission spectra. This approach, although straightforward, demonstrated promising results in terms of relative thermal sensitivity and temperature uncertainty, making it a viable option for temperature monitoring. We conclude that the morphology of the nanomaterials does not impact significantly on their thermometric performance. In the literanalyzingature dissimilar results were reported.[67–69] Alencar et al.[67] observe that as the $BaTiO_3$:Er3 nanocrystals decrease (from 60 to 26 nm) S_r increases. Marciniak et al.[69,70] found a similar tendency in $NaYF_4$:Yb^{3+}/Er^{3+} and $LiLaP_4O_{12}$:Yb^{3+}/Er^{3+} nanophosphors as the size of the nanocrystals decreases from 240 to 20 nm. An opposite trend was reported by Dong et al.[68] on $NaYF_4$:Yb^{3+}/Er^{3+} microspheres (size from 0.7 to 2 μm) showing that the thermal sensitivity decreases as size increases, reaching a maximum value at 223 K. Intriguingly, both trends were attributed to the larger specific surface area of the smaller crystals. As the size of the crystal decreases, a relatively large number of optically active ions are located at the surface and its contribution becomes increasingly important, being influenced by non-radiative relaxation channels related to electron–phonon interactions that are stronger with increasing temperature.[67–69] Moreover, the non-radiative rates of the two emitting levels might present a distinct temperature dependence and when the size of the nanoparticle decreases the material's phonons

density changes inducing a dependence of those rates with the crystal size. However, Balabhadra *et al.*[71] and Brandão-Silva *et al.*[72] do not observe significant changes on S_r values with the decrease of the particle size in SrF_2:Yb^{3+}/Er^{3+} (size from 10 to 41 nm) and Y_2O_3:Er^{3+} (21 to 86 nm) NPs, respectively. In this work, the surface area does not impact the performance of the luminescent WeS_2 QDs and NRs thermometers, and the surface-to-volume ratio remains unaltered in our samples, around 10^9 m^{-1}, corroborating the central role of the surface-to-volume ratio on the deactivation mechanism in luminescent materials.

Inspired by recent advancements in MLR analysis, we applied this methodology to our emission data. As a result, we observe an enhanced sensitivity and reduced temperature uncertainty, offering a ten-fold improvement in relative thermal sensitivity. This highlights the potential of MLR as a valuable tool for advancing luminescent nanothermometry. Moreover, our reproducibility assessments demonstrated the high thermal stability of the prepared materials suggesting their suitability for multiple uses as nanothermometers. In the rapidly evolving landscape of nanoscale temperature sensing, our findings on the luminescent properties of WSe_2 nanomaterials offer a promising avenue for the development of highly accurate and sensitive luminescence thermometry techniques, with potential applications spanning from materials science to biomedical research and beyond.

Author contributions

PMM: formal analysis and investigation, writing – original draft. MAHR: formal analysis and investigation. CDSB: conceptualization, data curation, investigation, methodology, supervision, validation writing. JCP: formal analysis and investigation. RA: conceptualization, methodology, supervision, writing – review & editing. JN: conceptualization, funding acquisition, methodology, supervision, validation, writing – review & editing.

Conflicts of interest

There are no conflicts to declare.

Acknowledgements

References

1 M. Chhowalla, H. S. Shin, G. Eda, L. J. Li, K. P. Loh and H. Zhang, *Nat. Chem.*, 2013, **5**, 263–275.
2 T. Ahmed, J. J. Zha, K. K. H. Lin, H. C. Kuo, C. L. Tan and D. H. Lien, *Adv. Mater.*, 2023, **35**, 2208054.
3 D. Lee, H. Jeong, H. Lee, Y. H. Kim and J. Y. Park, *Small*, 2023, **19**, 2302713.
4 M. L. Gao, L. X. Yu, Q. Lv, F. Y. Kang, Z. H. Huang and R. T. Lv, *J. Materiomics*, 2023, **9**, 768–786.
5 P. H. Ci, Y. B. Chen, J. Kang, R. Suzuki, H. S. Choe, J. Suh, C. Ko, T. Park, K. Shen, Y. Iwasa, S. Tongay, J. W. Ager, L. W. Wang and J. Q. Wu, *Nano Lett.*, 2017, **17**, 4982–4988.
6 G. H. Han, D. L. Duong, D. H. Keum, S. J. Yun and Y. H. Lee, *Chem. Rev.*, 2018, **118**, 6297–6336.
7 Q. H. Wang, K. Kalantar-Zadeh, A. Kis, J. N. Coleman and M. S. Strano, *Nat. Nanotechnol.*, 2012, **7**, 699–712.
8 W. C. Jin, P. C. Yeh, N. Zaki, D. T. Zhang, J. T. Sadowski, A. Al-Mahboob, A. M. van der Zande, D. A. Chenet, J. I. Dadap, I. P. Herman, P. Sutter, J. Hone and R. M. Osgood, *Phys. Rev. Lett.*, 2013, **111**, 106801.
9 H. R. Gutierrez, N. Perea-Lopez, A. L. Elias, A. Berkdemir, B. Wang, R. Lv, F. Lopez-Urias, V. H. Crespi, H. Terrones and M. Terrones, *Nano Lett.*, 2013, **13**, 3447–3454.
10 K. F. Mak, C. Lee, J. Hone, J. Shan and T. F. Heinz, *Phys. Rev. Lett.*, 2010, **105**, 136805.
11 A. Kuc, N. Zibouche and T. Heine, *Phys. Rev. B: Condens. Matter Mater. Phys.*, 2011, **83**, 245213.
12 N. Choudhary, M. R. Islam, N. Kang, L. Tetard, Y. Jung and S. I. Khondaker, *J. Phys.: Condens.Matter*, 2016, **28**, 364002.
13 D. Monga, S. Sharma, N. P. Shetti, S. Basu, K. R. Reddy and T. M. Aminabhavi, *Mater. Today Chem.*, 2021, **19**, 100399.
14 D. Jariwala, V. K. Sangwan, L. J. Lauhon, T. J. Marks and M. C. Hersam, *ACS Nano*, 2014, **8**, 1102–1120.
15 C. D. S. Brites, R. Marin, M. Suta, A. N. C. Neto, E. Ximendes, D. Jaque and L. D. Carlos, *Adv. Mater.*, 2023, **35**, 2302749.
16 D. Jaque and F. Vetrone, *Nanoscale*, 2012, **4**, 4301–4326.
17 C. D. S. Brites, A. Millán and L. D. Carlos, in *Handbook on the Physics and Chemistry of Rare Earths*, ed. J.-C. G. Bünzli and V. K. Pecharsky, Elsevier Science, B. V., Amsterdam, 2016, ch. 281, vol. 49, pp. 339–427.
18 U. Lucia, G. Grazzini, B. Montrucchio, G. Grisolia, R. Borchiellini, G. Gervino, C. Castagnoli, A. Ponzetto and F. Silvagno, *Sci. Rep.*, 2015, **5**, 11587.
19 M. Monti, L. Brandt, J. Ikomikumm and H. Olsson, *Scand. J. Haematol.*, 1986, **36**, 353–357.
20 M. Kallerhoff, M. Karnebogen, D. Singer, A. Dettenbach, U. Gralher and R. H. Ringert, *Urol. Res.*, 1996, **24**, 83–91.

21 R. Brown and P. Rickless, *Proc. R. Soc. London, Ser. B*, 1949, **136**, 110–125.

22 P. Wust, B. Hildebrandt, G. Sreenivasa, B. Rau, J. Gellermann, H. Riess, R. Felix and P. M. Schlag, *Lancet Oncol.*, 2002, **3**, 487–497.

23 X. D. Zhang, H. S. Wang, A. L. Antaris, L. L. Li, S. Diao, R. Ma, A. Nguyen, G. S. Hong, Z. R. Ma, J. Wang, S. J. Zhu, J. M. Castellano, T. Wyss-Coray, Y. Y. Liang, J. Luo and H. J. Dai, *Adv. Mater.*, 2016, **28**, 6872–6879.

24 A. L. Antaris, H. Chen, K. Cheng, Y. Sun, G. S. Hong, C. R. Qu, S. Diao, Z. X. Deng, X. M. Hu, B. Zhang, X. D. Zhang, O. K. Yaghi, Z. R. Alamparambil, X. C. Hong, Z. Cheng and H. J. Dai, *Nat. Mater.*, 2016, **15**, 235–242.

25 B. H. Lee, R. L. McKinney, M. T. Hasan and A. V. Naumov, *Materials*, 2021, **14**, 616.

26 P. Haro-Gonzalez, W. T. Ramsay, L. M. Maestro, B. del Rosal, K. Santacruz-Gomez, M. D. Iglesias-de la Cruz, F. Sanz-Rodriguez, J. Y. Chooi, P. R. Sevilla, M. Bettinelli, D. Choudhury, A. K. Kar, J. G. Sole, D. Jaque and L. Paterson, *Small*, 2013, **9**, 2162–2170.

27 L. Shang, F. Stockmar, N. Azadfar and G. U. Nienhaus, *Angew. Chem., Int. Ed.*, 2013, **52**, 11154–11157.

28 G. S. Terentyuk, A. V. Ivanov, N. I. Polyanskaya, I. L. Maksimova, A. A. Skaptsov, D. S. Chumakov, B. N. Khlebtsov and N. G. Khlebtsov, *Quantum Electron.*, 2012, **42**, 380–389.

29 B. del Rosal, A. Perez-Delgado, M. Misiak, A. Bednarkiewicz, A. S. Vanetsev, Y. Orlovskii, D. J. Jovanovic, M. D. Dramicanin, U. Rocha, K. U. Kumar, C. Jacinto, E. Navarro, E. M. Rodriguez, M. Pedroni, A. Speghini, G. A. Hirata, I. R. Martin and D. Jaque, *J. Appl. Phys.*, 2015, **118**, 143104.

30 S. Balabhadra, M. L. Debasu, C. D. S. Brites, J. Rocha and L. D. Carlos, *J. Lumin.*, 2016, **180**, 25–30.

31 C. Gota, K. Okabe, T. Funatsu, Y. Harada and S. Uchiyama, *J. Am. Chem. Soc.*, 2009, **131**, 2766–2767.

32 K. Okabe, N. Inada, C. Gota, Y. Harada, T. Funatsu and S. Uchiyama, *Nat. Commun.*, 2012, **3**(705).

33 J. J. Zhou, B. del Rosal, D. Jaque, S. Uchiyama and D. Y. Jin, *Nat. Methods*, 2020, **17**, 967–980.

34 F. Urbach, N. R. Nail and D. Pearlman, *J. Opt. Soc. Am.*, 1949, **39**, 1011–1019.

35 L. C. Bradley, *Rev. Sci. Instrum.*, 1953, **24**, 219–220.

36 R. N. Lawson, *Ann. N. Y. Acad. Sci.*, 1964, **121**, 31–33.

37 B. Han, W. L. Hanson, K. Bensalah, A. Tuncel, J. M. Stern and J. A. Cadeddu, *Ann. Biomed. Eng.*, 2009, **37**, 1230–1239.

38 L. M. Maestro, E. M. Rodriguez, F. S. Rodriguez, M. C. I. la Cruz, A. Juarranz, R. Naccache, F. Vetrone, D. Jaque, J. A. Capobianco and J. G. Sole, *Nano Lett.*, 2010, **10**, 5109–5115.

39 B. L. Vallee and D. D. Ulmer, *Annu. Rev. Biochem.*, 1972, **41**, 91–128.

40 A. Benayas, F. Q. Ren, E. Carrasco, V. Marzal, B. del Rosal, B. A. Gonfa, A. Juarranz, F. Sanz-Rodriguez, D. Jaque, J. Garcia-Sole, D. L. Ma and F. Vetrone, *Adv. Funct. Mater.*, 2015, **25**, 6650–6659.

41 Y. L. Shen, H. D. A. Santos, E. C. Ximendes, J. Lifante, A. Sanz-Portilla, L. Monge, N. Fernandez, I. C. Coria, C. Jacinto, C. D. S. Brites, L. D. Carlos, A. Benayas, M. C. Iglesias-de la Cruz and D. Jaque, *Adv. Funct. Mater.*, 2020, **30**, 2002730.

42 H. D. A. Santos, D. Ruiz, G. Lifante, C. Jacinto, B. H. Juarez and D. Jaque, *Nanoscale*, 2017, **9**, 2505–2513.

43 R. Z. Liang, R. Tian, W. Y. Shi, Z. H. Liu, D. P. Yan, M. Wei, D. G. Evans and X. Duan, *Chem. Commun.*, 2013, **49**, 969–971.

44 F. E. Maturi, C. D. S. Brites, E. C. Ximendes, C. Mills, B. Olsen, D. Jaque, S. J. L. Ribeiro and L. D. Carlos, *Laser Photonics Rev.*, 2021, **15**(2100301).

45 S. Zanella, M. Aragon-Alberti, C. D. S. Brite, F. Salles, L. D. Carlos and J. R. M. Long, *Angew. Chem., Int. Ed.*, 2023, DOI: **10.1002/anie.202306970**.

46 E. Ximendes, R. Marin, L. D. Carlos and D. Jaque, *Light: Sci. Appl.*, 2022, **11**(237).

47 E. L. K. Chng and M. Pumera, *RSC Adv.*, 2015, **5**, 3074–3080.

48 D. Singh, A. Singh, S. K. Ojha and A. K. Ojha, *Synth. Met.*, 2023, **293**, 117263.

49 S. P. Anubhav, G. Hautier, W. Chen, W. D. Richards, S. Dacek, S. Cholia, D. Gunter, D. Skinner, G. Ceder and K. A. Persson, APL Mater., 2013, **1**, 011002.

50 J. Y. Ding, Z. T. Liu, Z. Huang, Z. C. Jiang, Y. C. Yang, Z. H. Liu, J. S. Liu, Y. F. Guo and D. W. Shen, *Tungsten*, 2023, **5**, 350–356.

51 J. Z. Ding, A. L. Feng, X. D. Li, S. J. Ding, L. Liu and W. Ren, *J. Phys. D: Appl. Phys.*, 2021, **54**, 173002.

52 H. Nie, M. J. Li, Q. S. Li, S. J. Liang, Y. Y. Tan, L. Sheng, W. Shi and S. X. A. Zhang, *Chem. Mater.*, 2014, **26**, 3104–3112.

53 B. L. Li, L. X. Chen, H. L. Zou, J. L. Lei, H. Q. Luo and N. B. Li, *Nanoscale*, 2014, **6**, 9831–9838.

54 S. J. Xu, D. Li and P. Y. Wu, *Adv. Funct. Mater.*, 2015, **25**, 1127–1136.

55 Y. Li, Y. Hu, Y. Zhao, G. Q. Shi, L. E. Deng, Y. B. Hou and L. T. Qu, *Adv. Mater.*, 2011, **23**, 776–780.

56 J. Peng, W. Gao, B. K. Gupta, Z. Liu, R. Romero-Aburto, L. H. Ge, L. Song, L. B. Alemany, X. B. Zhan, G. H. Gao, S. A. Vithayathil, B. A. Kaipparettu, A. A. Marti, T. Hayashi, J. J. Zhu and P. M. Ajayan, *Nano Lett.*, 2012, **12**, 844–849.

57 W. Gu, Y. H. Yan, X. N. Cao, C. L. Zhang, C. P. Ding and Y. Z. Xian, *J. Mater. Chem. B*, 2016, **4**, 27–31.

58 D. Gopalakrishnan, D. Damien, B. Li, H. Gullappalli, V. K. Pillai, P. M. Ajayan and M. M. Shaijumon, *Chem. Commun.*, 2015, **51**, 6293–6296.

59 A. Bora, L. P. L. Mawlong, R. Das and P. K. Giri, *J. Colloid Interface Sci.*, 2020, **561**, 519–532.

60 K. Oreszczuk, T. Kazimierczuk, T. Smolenski, K. Nogajewski, A. Grzeszczyk, A. Lopion, M. Potemski and P. Kossacki, *Phys. Rev. B*, 2020, **102**, 245409.

61 C. Y. Wang, X. B. Liu, Q. Chen, D. Q. Chen, Y. X. Wang and S. Meng, *Phys. Rev. Lett.*, 2023, **131**, 245409.

62 M. Massicotte, F. Vialla, P. Schmidt, M. B. Lundeberg, S. Latini, S. Haastrup, M. Danovich, D. Davydovskaya, K. Watanabe, T. Taniguchi, V. I. Fal'ko, K. S. Thygesen, T. G. Pedersen and F. H. L. Koppens, *Nat. Commun.*, 2018, **9**, 066401.

63 Y. M. You, X. X. Zhang, T. C. Berkelbach, M. S. Hybertsen, D. R. Reichman and T. F. Heinz, *Nat. Phys.*, 2015, **11**, 477-U138.

64 T. Y. Jeong, B. M. Jin, S. H. Rhim, L. Debbichi, J. Park, Y. D. Jang, H. R. Lee, D. H. Chae, D. Lee, Y. H. Kim, S. Jung and K. J. Yee, *ACS Nano*, 2016, **10**, 5560–5566.

65 J. F. Suyver, J. J. Kelly and A. Meijerink, *J. Lumin.*, 2003, **104**, 187–196.

66 P. S. Zhou, G. Collins, Z. Hens, K. M. Ryan, H. Geaney and S. Singh, *Nanoscale*, 2020, **12**, 22307–22316.

67 M. A. R. C. Alencar, G. S. Maciel, C. B. de Araújo and A. Patra, *Appl. Phys. Lett.*, 2004, **84**, 4753–4755.

68 B. Dong, R. N. Hua, B. S. Cao, Z. P. Li, Y. Y. He, Z. Y. Zhang and O. S. Wolfbeis, *Phys. Chem. Chem. Phys.*, 2014, **16**, 20009–20012.

69 Ł. Marciniak, K. Prorok and A. Bednarkiewicz, *J. Mater. Chem. C*, 2017, **5**, 7890–7897.

70 Ł. Marciniak, A. Bednarkiewicz and W. Strek, *Sens. Actuators, B*, 2017, **238**, 381–386.

71 S. Balabhadra, M. L. Debasu, C. D. S. Brites, R. A. S. Ferreira and L. D. Carlos, *J. Phys. Chem. C*, 2017, **121**, 13962–13968.

72 A. C. Brandão-Silva, M. A. Gomes, S. M. V. Novais, Z. S. Macedo, J. F. M. Avila, J. J. Rodrigues and M. A. R. C. Alencar, *J. Alloys Compd.*, 2018, **731**, 478–488.